**PAPER**

# Outward particle transport by coherent mode in the H-mode pedestal in the Experimental Advanced Superconducting Tokamak (EAST)

To cite this article: T Zhang *et al* 2017 *Plasma Phys. Control. Fusion* **59** 065012

View the article online for updates and enhancements.

## Related content

- Experimental study of pedestal turbulence on EAST tokamak
  X. Gao, T. Zhang, X. Han et al.

- Excitation of edge plasma instabilities and their role in pedestal saturation in the HL-2A tokamak
  W L Zhong, X L Zou, Z B Shi et al.

- Enhanced-recycling H-mode regimes with edge coherent modes achieved by RF heating with lithium-wall conditioning in the EAST superconducting tokamak
  H.Q. Wang, G.S. Xu, H.Y. Guo et al.

## Recent citations

- Effect of pedestal fluctuation on ELM frequency in the EAST tokamak
  F.B. Zhong *et al*

- Divertor heat flux simulations in ELMy H-mode discharges of EAST
  T.Y. Xia *et al*

# Outward particle transport by coherent mode in the H-mode pedestal in the Experimental Advanced Superconducting Tokamak (EAST)

T Zhang[1], X Han[1,4], X Gao[1,2,4], H Q Liu[1], T H Shi[1], J B Liu[1], Y Liu[1], D F Kong[1], Z X Liu[1], H Qu[1], H M Xiang[1,3], K N Geng[1], Y M Wang[1], F Wen[1], S B Zhang[1], B L Ling[1] and the EAST team

[1] Institute of Plasma Physics, Chinese Academy of Sciences, PO Box 1126, Hefei, Anhui 230031, People's Republic of China
[2] School of Nuclear Science and Technology, University of Science and Technology of China, Hefei 230026, People's Republic of China
[3] College of Physics and Energy, Shenzhen University, Shenzhen 518060, Guangdong Province, People's Republic of China

E-mail: Hanx@ipp.ac.cn and xgao@ipp.ac.cn

CrossMark

## Abstract

A coherent mode (CM) in the edge pedestal region has been observed on different fluctuation quantities, including density fluctuation, electron temperature fluctuation and magnetic fluctuation in H mode plasma on the Experimental Advanced Superconducting Tokamak (EAST) tokamak. Measurements at different poloidal positions show that the local poloidal wavenumber is smallest at the outboard midplane and will increase with poloidal angle. This poloidal asymmetry is consistent with the flute-like assumption (i.e. $k_{//} \sim 0$) from which the toroidal mode number of the mode has been estimated as between 12 and 17. It was further found that the density fluctuation amplitude of the CM also demonstrated poloidal asymmetry. The appearance of a CM can clearly decrease or even stop the increase in the edge density, while the disappearance of a CM will lead to an increase in the pedestal density and density gradient. Statistical analysis showed there was a trend that as the CM mode amplitude increased, the rate of increase of the edge density decreased and the particle flux ($\Gamma_{\mathrm{div}}$) onto the divertor plate increased. The CM sometimes showed burst behavior, and these bursts led bursts on $\Gamma_{\mathrm{div}}$ with a time of about 230 $\mu$s, which is close to the time for particle flow from the outer midplane to the divertor targets along the scrape-off layer magnetic field line. This evidence showed that the CM had an effect on the outward transport of particles.

Keywords: pedestal, coherent mode, pedestal particle transport

(Some figures may appear in colour only in the online journal)

## 1. Introduction

It is well known that the H-mode pedestal plays a central role in achieving a high performance plasma [1–3], thus an understanding of the transport process in the pedestal region is important for prediction and further improvement of pedestal confinement. It is believed that the improvement in confinement in the H-mode is due to the suppression of turbulence in the edge. The results from transport analyses, however, suggested that there was remnant turbulence-

---

[4] Authors to whom any correspondence should be addressed.

induced transport in the pedestal region [4, 5]. The experimental results in DIII-D [6, 7] and ASDEX-Upgrade (AUG) [8] showed that the pedestal pressure gradient recovered quickly after an edge-localized mode (ELM) crash and then saturated for a long time up to the next ELM crash. Electromagnetic turbulence, such as the kinetic ballooning mode (KBM), has been suggested to be responsible for this saturation of the pedestal gradient [7]. Based on the KBM and peeling–ballooning instabilities, a predictive model of pedestal height and width, EPED, has been developed [9]. This model predicts that the KBM limits the pedestal pressure gradient, while the peeling–ballooning instabilities limit the pedestal height. The two constraints determine the pedestal width. The pedestal height and width predicted by EPED have been successfully tested across multiple international tokamaks [10]. Gyrokinetic calculations on MAST indicate that both the KBM and the micro-tearing mode (MTM) determine pedestal evolution between type-I ELMs [11, 12]. A recent nonlinear gyrokinetic turbulence simulation has demonstrated that the combination of MTM and electron temperature gradient (ETG) turbulence, along with neoclassical transport, was sufficient to explain pedestal transport for the H-mode on JET with an ITER-like wall [13].

In recent years, experimental efforts have also been made to measure the fluctuations in the pedestal region and investigate whether these fluctuating modes play an important role in pedestal formation. High-frequency coherent (HFC) modes, with characteristics expected for KBMs, have been observed in the QH-mode pedestal region on DIII-D, and the appearance of HFC modes stops the pedestal pressure increasing [14]. Quasi-coherent fluctuations (QCFs) observed in Alcator C-Mod [15] and DIII-D [16] have the effect of saturating the pedestal electron temperature. High-frequency magnetic fluctuation above 200 kHz on AUG was correlated with the pedestal pressure saturation [17]. The quasi-coherent mode observed on HL-2A is driven by pedestal density gradient and in return regulates the evolution of pedestal density [18].

On the Experimental Advanced Superconducting Tokamak (EAST), a coherent mode (CM) was usually observed in the density fluctuation spectrum about several tens of milliseconds after L–H transition. A typical characteristic is that the mode frequency gradually decreases as the pedestal evolves. It is shown that a CM exists in the edge pedestal region just inside the separatrix [19]. Analysis also showed that the appearance of a CM is closely related to the pedestal electron pressure and suggests that the mode is a kind of pressure-driven instability [20]. However, some important characteristics of the mode, such as the poloidal distribution, have not yet been studied, and it was also not clear at that time whether the CM has the effect of regulating the pedestal transport. In this paper, the poloidal distribution of the CM will be documented and clear evidence that the CM can drive outward particle transport will also be presented. In the rest of this paper, the experimental setup is described in section 2; section 3 presents the poloidal distribution of the coherent mode; the evidence that CM can drive outward particle
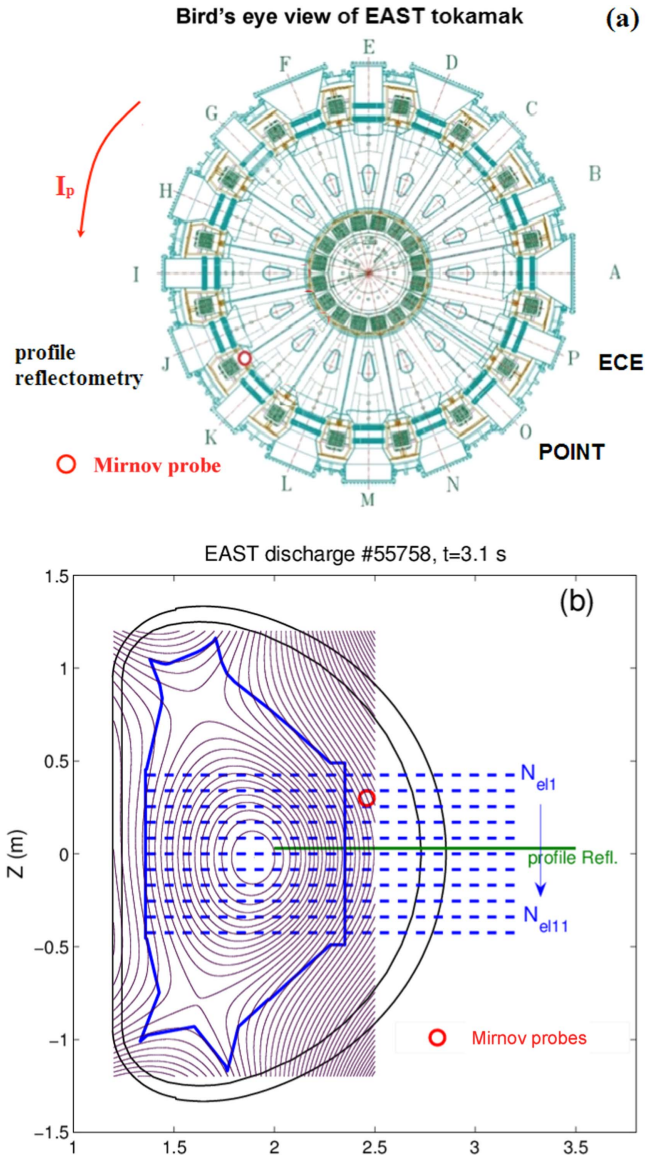


**Figure 1.** Toroidal view (a) and poloidal view (b) of the main diagnostics used for analysis.

transport is given in section 4; the results are discussed and summarized in section 5.

## 2. Experimental setup

EAST is a medium size superconducting tokamak with major radius $R_0 = 1.85$ m and minor radius $a = 0.45$ m. The plasmas in the present study were with plasma current $I_p = 380$–500 kA, toroidal magnetic field $B_T = 1.8$–2.5 T, $q_{95} = 5$–7 and mainly heated by radiofrequency waves, including lower hybrid wave (LHW), ion cyclotron resonance heating (ICRH) and electron cyclotron resonance heating (ECRH). These plasmas were usually accompanied by type-I ELMs in the H-mode phase. Figure 1 shows toroidal and poloidal views of the main diagnostics for analysis. The plasma current is in the anti-clockwise direction seen from the top of machine, while the toroidal magnetic field is in the

clockwise or anti-clockwise direction. The 11-channel POINT (POLarimeter-INTerferometer) diagnostics [21] at port O was used to measure the line-integrated densities and also to monitor the density fluctuations. As shown in figure 1(b), the 11 horizontal POINT channels are uniformly distributed from top to bottom (Z from 42.5 cm to −42.5 cm) in the same poloidal cross-section, and thus the vertical distance between adjacent beams is 8.5 cm. The laser used with these diagnostics has a radius of 2.78 cm and thus the diagnostics can respond to fluctuation with a poloidal wavenumber $k_\theta \leqslant 2/2.78 \sim 1.44\,\mathrm{cm}^{-1}$. In the experiment, the sampling frequency of POINT diagnostics is 250 kHz, and therefore a fluctuation mode with frequency up to 125 kHz can be measured. In this paper, the line-integrated densities measured by POINT will be called $N_{\mathrm{el}1}$ to $N_{\mathrm{el}11}$. A multichannel middle-plane electron cyclotron emission (ECE) diagnostics [22] at port P was used to monitor the electron temperature and temperature fluctuations. The density profile was measured by a fast frequency-sweeping reflectometry [23–25] which has a horizontal view about 3 cm above the low-field side (LFS) midplane at port J. The magnetic fluctuations were measured by Mirnov probes mounted on the vacuum vessel wall.

## 3. Poloidal distribution of the CM

The CM can generally be observed in the spectrum of the line-integrated density signal measured by POINT diagnostics. Figure 2(a) shows a typical H-mode discharge (55758) heated by 2.5 MW, 4.6 GHz LHW and 0.5 MW ICRH. The plasma enters the H-mode phase at about 2.75 s, after which the line-averaged density ($\langle n_{\mathrm{e}} \rangle$) and diamagnetic energy ($W_{\mathrm{dia}}$) show rapid increases. The CM can be observed in all the POINT channels in the H-mode phase but only the spectrum of the middle channel ($N_{\mathrm{el}6}$) is shown here. The mode frequency shows sweeping-down characteristics roughly in the increasing phase of $\langle n_{\mathrm{e}} \rangle$ and $W_{\mathrm{dia}}$ and then saturates at a nearly stable value (23 kHz for the discharge of this figure). The appearance of an ELM can interrupt the CM but the later pedestal recovery will bring out the mode again. Besides the density fluctuation, the CM is also usually observed in the electron temperature fluctuation measured by the edge channels of ECE diagnostics, as shown in figure 2(b). The magnetic fluctuation measured by the Mirnov probe, however, cannot usually observe the CM. Nevertheless, several discharges with CM in the magnetic fluctuation have been found in the several hundred H-mode plasmas analyzed and significant coherence between magnetic and density fluctuation was actually observed. The selected discharge 55758 is one such plasma. As shown in figure 2(b), the coherence spectrum between the Mirnov signal and $N_{\mathrm{el}2}$ clearly shows the CM mode structure. It is further found that the magnetic probes located in the LFS can observe the CM while the high-field side probes cannot observe the mode. This implies that the mode has a ballooning structure. Previous results [19] show that the CM is mainly observed in the edge pedestal region. Therefore, the measurement by the
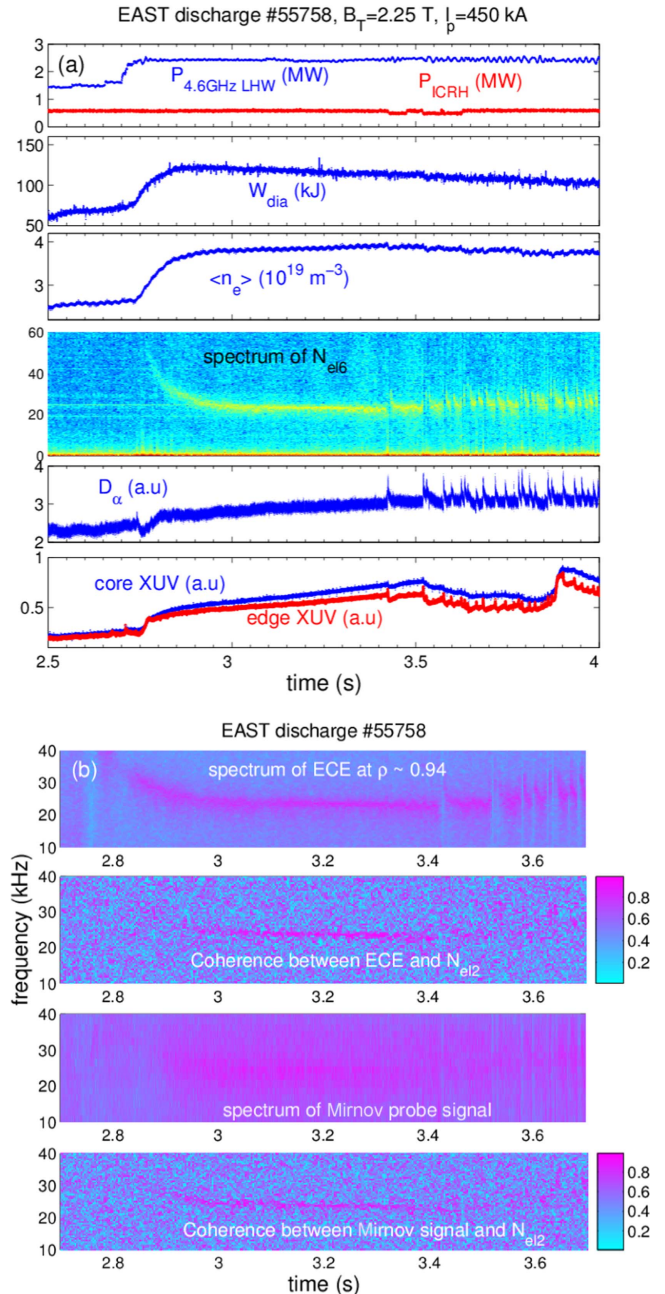


**Figure 2.** (a) Observation of a CM by the horizontal interferometer (POINT) in an EAST H-mode plasma. (b) Spectra of ECE and Mirnov signals and the coherence between them and interferometer signal.

horizontal interferometer mainly reflects the density fluctuation localized at the edge pedestal region of the LFS.

From the measurement by POINT diagnostics at different poloidal positions, the poloidal distributions of the wavenumber and density fluctuation level for the CM have been studied. The poloidal wavenumbers ($k_\theta$) of the CM have been estimated by applying correlation analysis in the frequency domain on the signals measured by each of two adjacent POINT laser beams. Figure 3(a) shows an example of such correlation analysis for [$N_{\mathrm{el}5}$, $N_{\mathrm{el}6}$] and [$N_{\mathrm{el}2}$, $N_{\mathrm{el}3}$] for discharge 55758. It is seen that the coherence at the CM mode frequency is very high, larger than 0.8. From this correlation
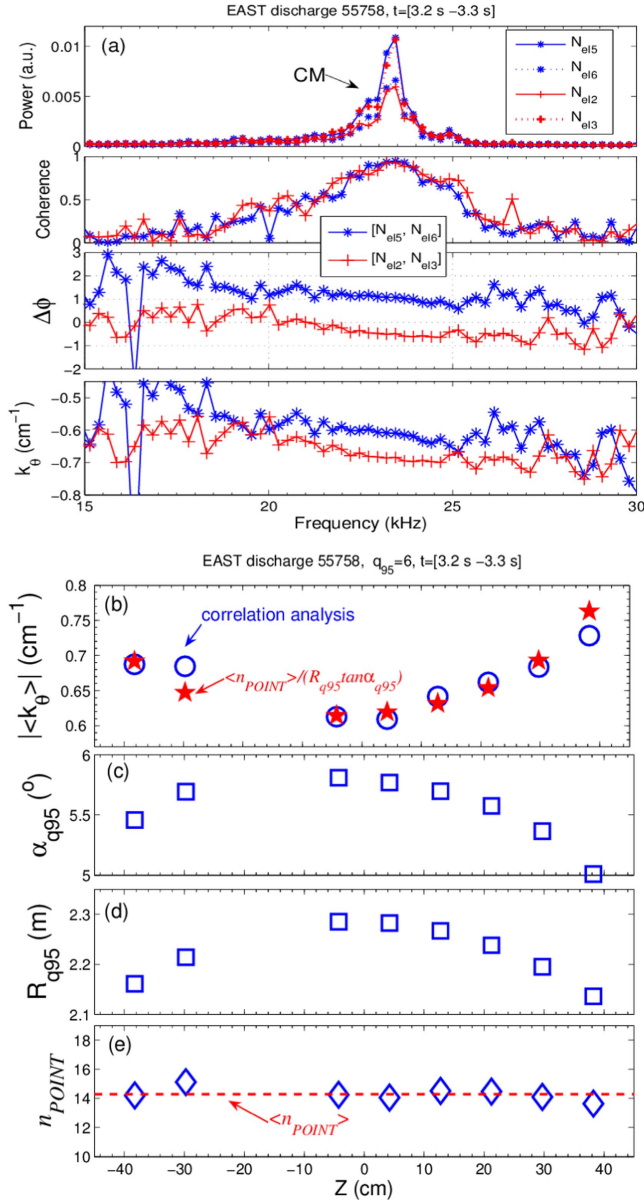
**Figure 3.** (a) The power spectra, coherence spectra, cross-phase spectra and deduced poloidal wavenumber for [$N_{el5}$, $N_{el6}$] and [$N_{el2}$, $N_{el3}$]. (b) The poloidal distributions of local $k_\theta$ deduced using direct correlation analysis (O) in (a) and the flute-like mode assumption (★). (c), (d) The poloidal distributions of local magnetic field pitch angle and the major radius of the CM at the intersection points between POINT diagnostics line views and $q_{95}$ surfaces at the LFS. (e) Estimated toroidal mode number from the POINT diagnostics ($n_{POINT}$) using a flute-like assumption and the horizontal dashed line indicating the mean value $\langle n_{POINT} \rangle$.

analysis, the spectra of phase difference ($\Delta\phi$) for each pair signals have been acquired. In order to estimate the poloidal distance for each pair of signals, we used the EFIT reconstructed equilibrium to determine the intersection points of POINT diagnostic line views and the $q_{95}$ surface at the LFS. Then the distance between each adjacent intersection point, $\Delta l_{q95}$, can be calculated and will be taken as the poloidal distance for each pair of signals. For the case in figure 3(a), the $\Delta l_{q95}$ for [$N_{el5}$, $N_{el6}$] and [$N_{el2}$, $N_{el3}$] is 8.5 cm and 10 cm, respectively. The previous results in [20] showed that the

poloidal wavenumber of a CM close to the midplane is about 0.5–0.7 cm$^{-1}$, corresponding to a wavelength of 9–12.5 cm. In our present analysis using POINT diagnostics, the minimum poloidal distance (8.5 cm) has exceeded the half-wavelength of the CM and the $\Delta\phi$ acquired from the correlation analysis in figure 3(a) cannot reflect the right phase difference but should be corrected by $\pm 2\pi$. By considering that the CM rotates in the electron diamagnetic drift direction, a $-2\pi$ phase correction is applied to all the data and then the poloidal wavenumber can be estimated as $k_\theta = (\Delta\phi - 2\pi)/\Delta l_{q95}$ as shown in figure 3(a), where the negative value of $k_\theta$ indicates that the mode rotates in the electron diamagnetic drift direction. From the $k_\theta$ spectra, we take a mean value of $k_\theta$ in a specific frequency range as the local poloidal wavenumber ($\langle k_\theta \rangle$) for CM. Here, the power spectra in figure 3(a) are used to determine the specific frequency range for which the power is larger than $\exp(-1)$ of the maximum power for a CM. This calculation gives $\langle k_\theta \rangle$ for [$N_{el5}$, $N_{el6}$] and [$N_{el2}$, $N_{el3}$] of about $-0.6$ cm$^{-1}$ and $-0.68$ cm$^{-1}$, respectively, for the example shown in figure 3(a).

By doing a similar analysis to other adjacent POINT signals, the poloidal distribution of the absolute value of local poloidal wavenumber ($|\langle k_\theta \rangle|$) for the CM has been acquired in figure 3(b) where the x-axis is the mean value of the Z coordinates for each two adjacent POINT channels. It is that noted the eighth channel of the POINT diagnostics, i.e. $N_{el8}$, is broken in these shots and so the $|\langle k_\theta \rangle|$ from [$N_{el7}$, $N_{el8}$] and [$N_{el8}$, $N_{el9}$] are not available. It is seen from figure 3(b) that $|\langle k_\theta \rangle|$ takes its lowest value of 0.6 cm$^{-1}$ at the midplane and then gradually increases with increasing Z value. This could be explained based on the assumption that the CM is a flute-like mode, i.e. the wavenumber parallel to the magnetic filed ($k_{//}$) is close to 0. This assumption leads to a relation between toroidal mode number ($n$) and local poloidal wavenumber, and has been used to estimate the ELM filament toroidal mode number [26]:

$$n = R_{mode} k_\theta \tan\alpha$$

where $R_{mode}$ is the major radius of the mode location and $\alpha$ is the pitch angle of the local magnetic field. For our present case, the two parameters will be estimated at the intersection points of the POINT diagnostics and $q_{95}$ surfaces at the LFS and named $R_{q95}$ and $\alpha_{q95}$, respectively. The poloidal distributions of the two parameters are shown in figures 3(c) and (d). Then the toroidal mode number of the CM can be estimated as $n_{POINT} = R_{q95}|\langle k_\theta \rangle| \tan\alpha_{q95}$ (shown in figure 3(e)). For this case, the mean value of $n_{POINT}$ ($\langle n_{POINT} \rangle$) is about 14.3 while the standard deviation is 0.43, only a 3% deviation. In order to check the poloidal asymmetry of $|\langle k_\theta \rangle|$ in figure 3(b), we use the value of $\langle n_{POINT} \rangle$, i.e. 14.3, to calculate the poloidal wavenumber with $k_\theta = \langle n_{POINT} \rangle/(R_{q95} \tan\alpha_{q95})$ and it is found that these values of $k_\theta$ are consistent with those deduced using the cross-correlation method. This indicates the poloidal asymmetry of $|\langle k_\theta \rangle|$ is mainly due to the asymmetry of $R_{q95}$ and $\alpha_{q95}$ and also implies that the flute-like mode assumption for the CM is reasonable. We have also made a similar analysis for other discharges and a database for $|\langle k_\theta \rangle|$ and $\langle n_{POINT} \rangle$ has been acquired. The statistical
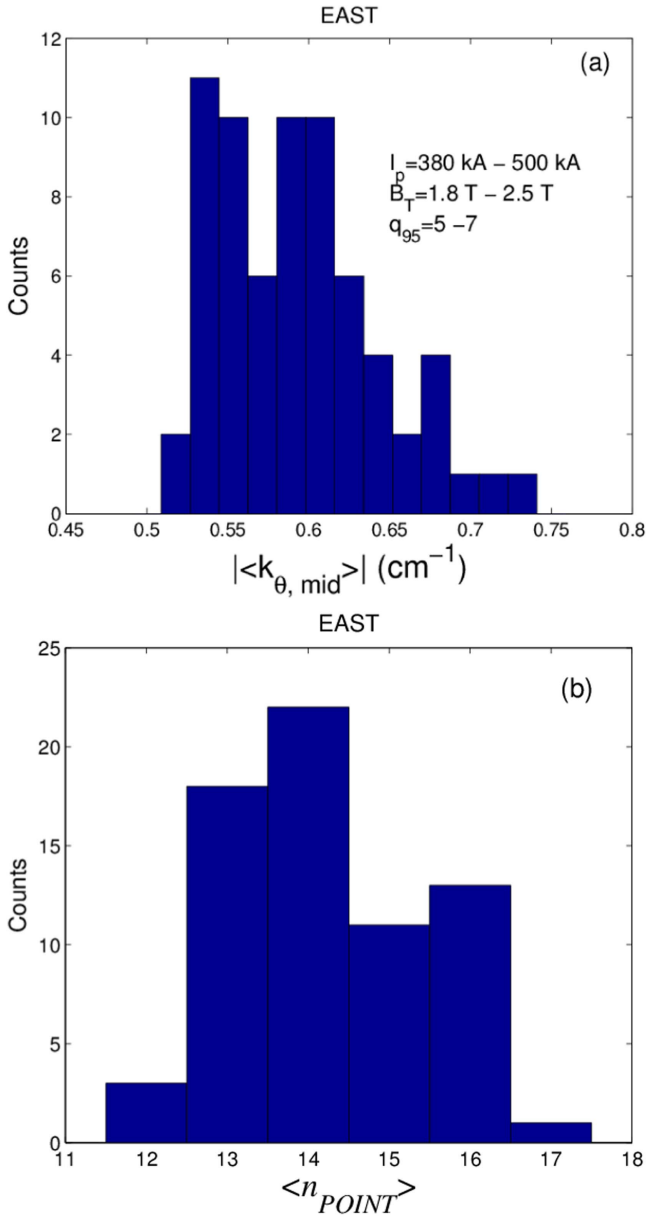
**Figure 4.** Statistical distribution of the poloidal wavenumber at midplane ($|\langle k_{\theta,\text{mid}}\rangle|$) and the estimated toroidal mode number ($\langle n_{POINT}\rangle$) for the CM for 68 EAST discharges.
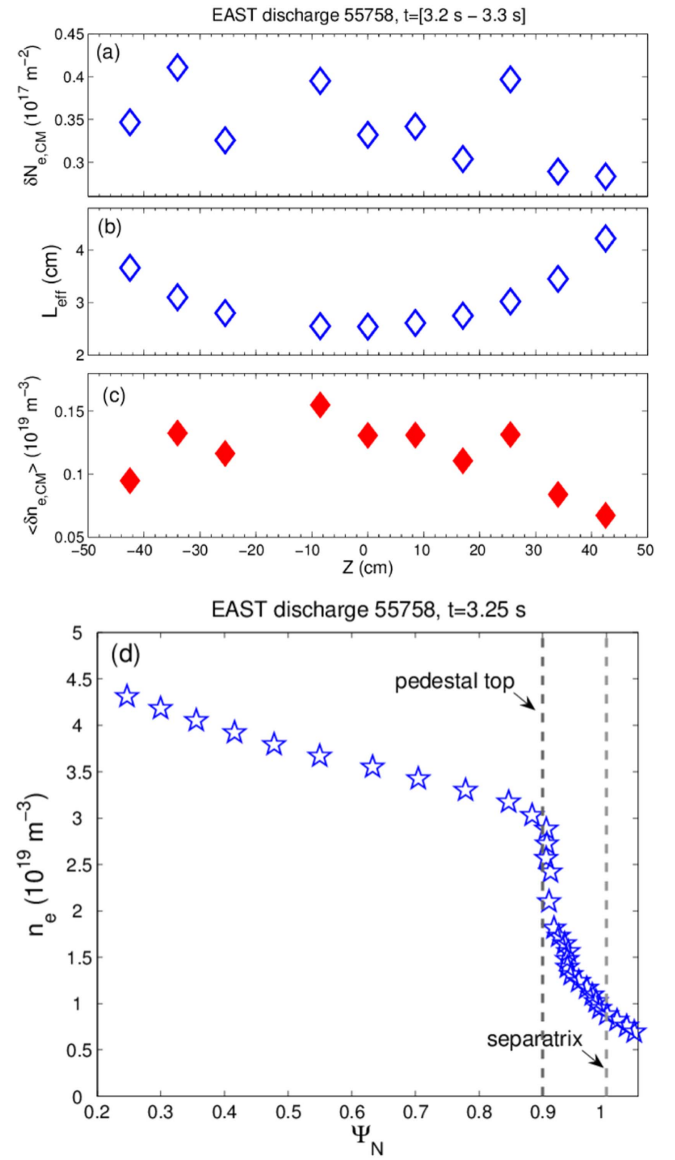


**Figure 5.** (a)–(c) Poloidal distributions of the line-integrated density fluctuation of the CM, the effective integrated length and the line-averaged density fluctuation of the CM, which are deduced from POINT measurements. (d) Density profiles for EAST discharge 55758 at $t = 3.25$ s; the vertical dashed lines indicate the pedestal top and separatrix.

distribution of $|\langle k_\theta\rangle|$ at the midplane ($|\langle k_{\theta,\text{mid}}\rangle|$) and $\langle n_{\text{POINT}}\rangle$ are shown in figure 4. It is seen that $|\langle k_{\theta,\text{mid}}\rangle|$ generally ranges from $0.5\,\text{cm}^{-1}$ to $0.75\,\text{cm}^{-1}$ and $\langle n_{\text{POINT}}\rangle$ is between 12 and 17.

Another interesting characteristic of the CM is the poloidal distribution of fluctuation amplitude. The POINT diagnostics directly measured the line-integrated density ($N_{\text{el}}$) and also the line-integrated density fluctuation level ($\delta N_{\text{el}}$). From POINT signals, we can directly calculate the line-integrated density fluctuation level of the CM ($\delta N_{\text{e,CM}}$) which has a relation to the local fluctuation level ($\delta n_{\text{e,CM}}$) as

$$\delta N_{\text{e,CM}} = \int \delta n_{\text{e,CM}}\,\text{d}l = \langle \delta n_{\text{e,CM}}\rangle L_{\text{eff}} \tag{1}$$

where $\langle \delta n_{\text{e,CM}}\rangle$ is the line-averaged density fluctuation level and $L_{\text{eff}}$ is the effective integrated length. Figure 5(a) has

shown the poloidal distribution of $\delta N_{\text{e,CM}}$ where the original data measured by POINT were first filtered by using a band-pass filter with a frequency range of 15–30 kHz, and then the standard deviation of the filtered signal was calculated and taken as $\delta N_{\text{e,CM}}$. It is seen from this plot that $\delta N_{\text{e,CM}}$ represents scattering along the poloidal direction. In order to calculate $\langle \delta n_{\text{e,CM}}\rangle$, $L_{\text{eff}}$ should be determined. As shown in [19], the CM exists in the edge pedestal region just inside the separatrix, and therefore the effective integrated region should be approximately from the pedestal top to the separatrix. Figure 5(d) shows the density profile in the poloidal flux coordinate ($\Psi_{\text{N}}$), and the pedestal top can be determined at about $\Psi_{\text{N}} = 0.9$ for this case. The intersection points of each
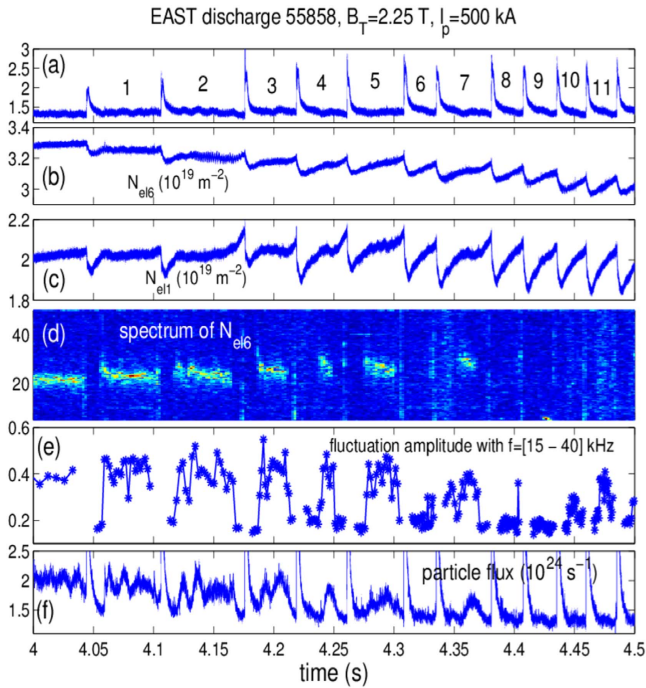
**Figure 6.** (a) Dα signal, with the numbers 1 to 11 indicating the 11 inter-ELM phases. (b) Line-integrated density at $Z = 0$, i.e. $N_{el6}$. (c) Line-integrated density at $Z = 42.5$ cm, i.e. $N_{el1}$. (d) Spectrum of $N_{el6}$. (e) The $N_{el6}$ fluctuation amplitude at the frequencies between 15 and 40 kHz. (f) The particle flux flowing onto the divertor.

POINT line view and $\Psi_N = 0.9/\Psi_N = 1$ surface can be determined using EFIT reconstructed equilibrium and then the distance of the two intersection points for each POINT channel is taken as $L_{eff}$, as shown in figure 5(b). It is seen that $L_{eff}$ at the midplane is about 2.5 cm, while it can reach 4.2 cm at $Z = 42.5$ cm, i.e. the uppermost POINT channel in figure 1(b). Then the line-averaged density fluctuation level $\langle \delta n_{e,CM} \rangle$ can be calculated according to equation (1), and is shown in figure 5(c). It can be observed that the value of $\langle \delta n_{e,CM} \rangle$ close to midplane is at about $0.14 \times 10^{19}$ m$^{-3}$ and shows a decreasing trend with increasing $Z$ value, e.g $\langle \delta n_{e,CM} \rangle \approx 0.06 \times 10^{19}$ m$^{-3}$ at $Z = 42.5$ cm, with a reduction of about 60% from that at midplane. As discussed at the beginning of this section, it is conjectured from the magnetic probe measurement that the CM has a ballooning structure. The result shown in figure 5(c) is further evidence for this conjecture.

## 4. Evidence of outward particle transport by the CM

In this section, we will present several lines of evidence that the CM can drive outward particle transport. As seen in figure 2, the CM can be also observed in the inter-ELM phase. The ELM can interrupt the CM but the mode will appear again in the pedestal recovery phase. It is usually observed that the edge density will stop increasing when the CM appears in this recovery phase. In addition, we also observe that the disappearance of the CM can lead to a further increase in edge density. The most representative discharge (55858) in

our database is shown in figure 6, where 11 complete inter-ELM phases, as indicated by the numbers 1 to 11 in figure 6(a), have been included. After each ELM crash, the edge density ($N_{el1}$) shows a fast increase. When a CM appears in the spectrum of density fluctuation (figure 6(d)), the edge density will stop increasing and even show a slight decrease, as seen for the inter-ELM phases 1–5 and 7 while $N_{el1}$ shows a continuous increase up to the next ELM for the other inter-ELM phases. Especially for the inter-ELM phases of 2–5 and 7, the CM disappears in the later phase and the edge density shows another increase up to the next ELM. We have checked other discharges in our database and found that the CM generally has the effect of reducing the rate of increase of the edge density. In order to show this relation, we chose four to five ELM cycles for each discharge in our database, decomposed each inter-ELM phase into three time intervals and calculated the corresponding CM mode amplitudes and the rates of increase in edge density, $dN_{el1}/dt$, for each interval. The result is shown in figure 7(a), where the normalized CM mode amplitude ($\delta N_{e,CM}/N_{el6}$) is calculated from the midplane POINT channel, i.e. $N_{el6}$. It can be observed that the rate of increase of edge density tends to decrease with increase in the mode amplitude. When the CM mode amplitude is large enough, $dN_{el1}/dt$ even takes a negative value, i.e. a density decrease.

The above result implies that the CM can drive outward particle transport. Additional evidence comes from the behavior of the particle flux onto the divertor ($\Gamma_{div}$), which is measured by divertor probes [27] and is shown in figure 6(f). By comparing the behaviors of $\Gamma_{div}$ and the CM, it is found that the existence of a CM in plasma corresponds to a higher divertor particle flux. The statistical relation between the divertor particle flux and the CM amplitude for the discharges in our database is summarized in figure 7(b). It can be seen that $\Gamma_{div}$ increases with increasing CM mode amplitude. If we look at the detailed evolution of the CM in the inter-ELM phase, we find that this mode usually shows a 'bursty' behavior. Figure 8(a) shows the signal and also the envelope of $N_{el6}$ after passing through a pass-band (15–40 kHz) filter for inter-ELM phase 5, and the bursty nature of the CM can be clearly observed. Here, the envelope of the density fluctuation ($\delta n(t)$) is calculated as follows: first a Hilbert transform is carried out on the density fluctuation signal, resulting a new time series of data $H(\delta n(t))$, and then the envelope ($E(t)$) is calculated by $E(t) = \sqrt{\delta n(t)^2 + [H(\delta n(t))]^2}$. The waveform of $\Gamma_{div}$ is also shown for comparison. It can be found that $\Gamma_{div}$ is increased after the appearance of the CM bursts; in particular the particle flux also presents bursts. An enlarged plot of figure 8(a) from 4.285 to 4.29 s is shown in figure 8(b). It can be observed that the CM bursts generally correspond to the $\Gamma_{div}$ bursts while former lead to the latter at about 200–300 $\mu$s in the time series, as indicated by the dashed lines. Figure 8(c) shows the cross-correlation function between the envelope of CM bursts and the particle flux for the phase from 4.276 s to 4.29 s. The largest cross-correlation coefficient is at a delay of $-230$ $\mu$s, indicating that the CM bursts lead to particle flux bursts at about 230 $\mu$s during the
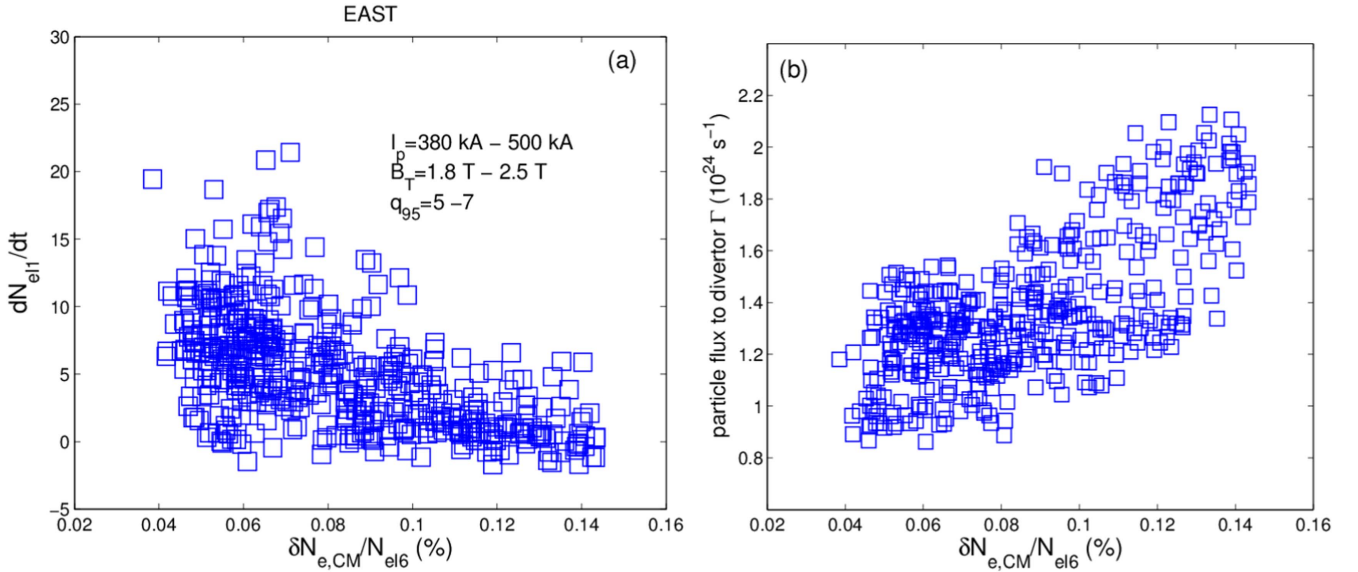
**Figure 7.** Statistical analysis of 68 EAST discharges for (a) the relation between the increasing rate of $N_{el1}$ and the normalized CM amplitude and (b) the relation between the particle flux onto the divertor and the normalized CM amplitude.

time phase. As discussed above, the CM has a ballooning structure and thus CM-induced particle flux will mainly spread out around the midplane of the LFS. Then the particles will flow from the outer midplane to the divertor targets on a time scale of the ion transit time ($\tau_{//}$) along the SOL magnetic field line. Here, $\tau_{//}$ can be estimated as $\tau_{//} \approx L_{//}/C_s$, with $L_{//} \approx \pi q_{95} R$ being the connection length and $C_s = [(T_e + T_i)/m_i]^{0.5}$ the ion sound speed. For our present case, $q_{95} = 5.6$, $T_e = T_i \approx 100\,\text{eV}$ and thus $L_{//} \approx 3.5\,\text{m}$, $C_s \approx 1 \times 10^5\,\text{m s}^{-1}$, gives $\tau_{//} \approx 350\,\mu\text{s}$. Therefore, the observed time delay (230 $\mu$s) between the CM bursts and the divertor particle flux bursts is actually close to the time for a particle to flow from ourter midplane to the divertor targets along the SOL magnetic field line.

Lastly, we will show how the CM influences the edge density profile. In our study, the edge density profile is measured by LFS reflectometry (figure 1) and fitted by a modified tanh function [28]

$$n_e = A \frac{(1 + \alpha z)e^z - (1 + \beta z)e^{-z}}{e^z + e^{-z}} + B$$

where

$$z = 2(X_{sym} - X)/w.$$

In the above function $X$ represents the real or flux coordinate of the density profile. $A$, $B$, $\alpha$, $\beta$, $X_{sym}$ and $w$ are five fitting parameters in which the density pedestal height $n_{e,ped}$ can be calculated by $n_{e,ped} = A + B$, $X_{sym}$ is the location of the barrier center and $w$ represents the width of the density pedestal. It is noted that the above fitting function has an additional fitting parameter $\beta$ to the function in [28]. This is because the density profile measured by reflectometry usually presents a density decay tail in the SOL region and the parameter $\beta$ can allow a smooth transition to the SOL density profile. The density pedestal height ($n_{e,ped}$) and the maximum absolute density gradient (max $|\nabla n_e|$) can be directly

calculated by fitting the density profiles measured by reflectometry. For the above analyzed typical discharge (55858) there is no density profile and we therefore chose another discharge (56201) for analysis. Figure 9 shows several inter-ELM phases for discharge 56201. The first inter-ELM phase from 3.48 s to 3.545 s is very similar to those of discharges 2–5 and 7 for 55858 shown in figure 6. The CM reappears at about 3.49 s after the ELM crash and the rate of increase of edge density $N_{el1}$ decreases while the CM disappears at about 3.532 s and $N_{el1}$ shows an increase again. Figures 9(d) and (e) show the behaviors of $n_{e,ped}$ and max $|\nabla n_e|$, respectively, with a time definition of 1 ms. It can be seen from the figure that the evolution of $n_{e,ped}$ is very similar to that of $N_{el1}$. Although the density gradient shows a large oscillation, its value is generally higher during the CM disappearance phase (3.532–3.545 s) than that at the CM prevailing phase (3.49–3.532 s). Figure 9(f) compares the density profiles in the two different phases. In order to reduce the random error, we choose the density profiles from 3.51 s to 3.52 s for the first phase and those from 3.54 s to 3.545 s for the second phase. The density profiles at each phase are put together and fitted by the above modified tanh function. It can be observed from figure 9(f) that both the density pedestal height and the gradient are higher during the phase without CM; in particular max $|\nabla n_e|$ (figure 9(g)) increases from $184 \times 10^{19}\,\text{m}^{-4}$ to $243 \times 10^{19}\,\text{m}^{-4}$, i.e. an increase of about 32%.

## 5. Discussion and summary

From the correlation analysis of CM in section 3, the mode phase velocity can be estimated. For the case in figure 3(a), the mode poloidal wavenumber at midplane is about 0.6 cm$^{-1}$ and the mode frequency is at about $f_{CM} = 23$ kHz. Then the mode phase velocity can be estimated as $V_{CM} \approx 2\pi f_{CM}/k_\theta = 2.4\,\text{km s}^{-1}$. The electron diamagnetic velocity

**Figure 9.** (a) Dα signal, (b) edge line-integrated density $N_{el1}$, (c) spectrum of core line-integrated density $N_{el6}$, (d) density pedestal height $n_{e,ped}$, (e) maximum of absolute pedestal density gradient, (f) density profiles with CM and without (w/o) CM and (g) the absolute density gradients with CM and w/o CM.
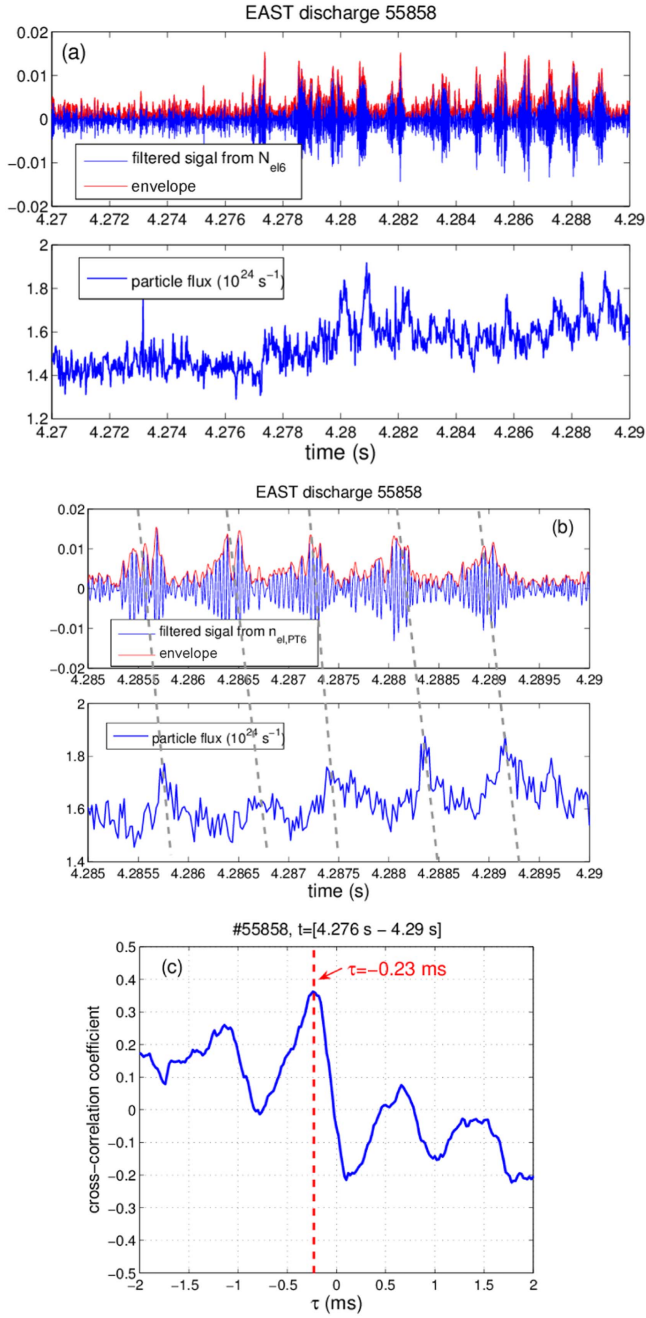


**Figure 8.** (a) Band-pass filtered signal of $N_{el6}$ and particle flux onto the lower divertor for the fifth inter-ELM phase in figure 5. (b) An enlarged plot for (a) from 4.285 to 4.29 s; the dashed lines show the delay between CM bursts and lower divertor particle flux bursts. (c) The cross-correlation function between the envelopes of CM bursts and particle flux bursts.

$V_e^* = \nabla p_e / enB$ at the edge pedestal gradient region was estimated as being between 10 and 30 km s$^{-1}$ and the ion diamagnetic velocity $V_i^*$ will be similar if we assume $T_i = T_e$ in the pedestal region since there is no $T_i$ profile measurement in pedestal region in our present studies. So the mode phase velocity is much smaller than the diamagnetic velocity. One possible explanation is as follows. The estimated $V_{CM}$ is in the machine frame and includes the contribution from $E \times B$ velocity from the radial electric field ($E_r$). Although there is as
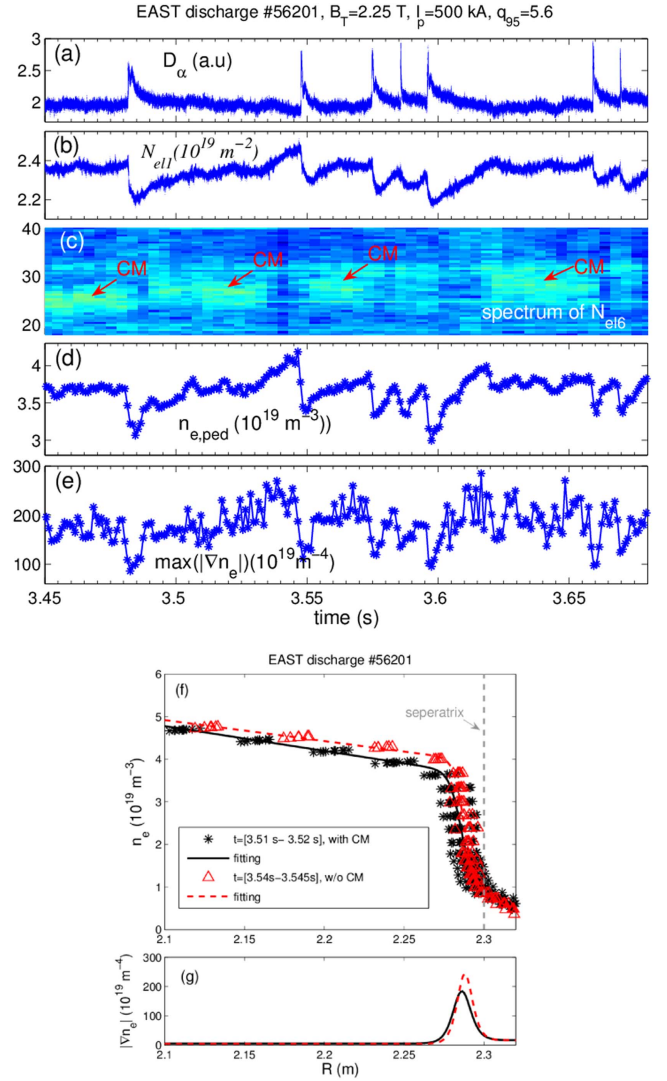
yet no $E_r$ measurement in the pedestal region on EAST, it is believed that the $E_r$ is similar to that of other machines, i.e. a negative $E_r$ well in the pedestal gradient region. If the CM rotates in the ion diamagnetic drift direction in the plasma frame, but with a value a little less than the $E \times B$ velocity, then the observed velocity in the machine frame, as seen in the experiment, will be in the electron diamagnetic drift direction but it will be much smaller than the diamagnetic velocity. In order to clarify this point, measurement of $E_r$ in pedestal region is necessary in the future on EAST.

In section 4 we showed that the CM mode is highly correlated with the rate of increase of edge density and the particle flux onto the divertor. In particular, the CM bursts lead to the particle flux bursts shown in figure 8. These results make us confident that the CM mode can drive outward particle flux. But the question is how large is the contribution of the CM to outward particle transport? It is seen from figure 6(f) that the particle flux onto the divertor during the

phase without CM (e.g. inter-ELM phases 8–11 ) has an average value of about $1.3 \times 10^{24} \, \text{s}^{-1}$, while the particle flux can be up to $2.1 \times 10^{24} \, \text{s}^{-1}$ during the phase with a CM. If the CM contributes to all the additional particle flux, the contribution of the CM can be up to about 38% of the total particle outward flux for the case shown in figure 6. It should be noted, however, there are possibilities that some other modes, which cannot be detected by the present diagnostics, could make a contribution to the outward particle flux. The main diagnostics for measuring density fluctuation in this paper is the horizontal interferometer (POINT) which can only respond to fluctuations with $k_\theta \leqslant 1.44 \, \text{cm}^{-1}$, as discussed in section 2. The CM mode is actually in the response range of this diagnostics. This would be next step to study the effect of fluctuation with higher mode numbers. In the present analysis, all the analyzed discharges have LHW heating and this precludes an analysis how the CM mode influences the fast dynamics of pedestal temperature by using ECE diagnostics. This will be left for future study.

Although we have confidence that the CM observed on EAST can enhance particle transport in the edge pedestal region, the transport mechanism is unclear at the moment. In fact, coherent structures in the pedestal region, which can enhance particle transport, have also been observed in other devices, such as the quasi-coherent mode (QCM) in the EDA H-mode on Alcator C-Mod [29] and the edge harmonic oscillations (EHO) in the quiescent H-mode (QH-mode) on DIII-D [30]. Langmuir probe measurement on QCM showed that this mode induced a particle flux due to $E \times B$ convection, $\Gamma = \langle \delta n \delta v_r \rangle$, comparable to the total fueling rate [31]. For EHO, it is speculated the EHO-induced particle transport is a function of edge rotation or edge rotation shear [32]. The recent nonlinear simulation for the DIII-D QH-mode has observed a saturated kink/peeling mode (KPM), which is thought to be a candidate EHO [33]. The simulation results showed that particle loss by KPM was mainly also due to $E \times B$ convection. It was also found that the appearance of a KPM can significantly increase the mean $E \times B$ flow due to Maxwell stress. This implies a very complex interaction between KPM and plasma flow, and this interaction should have effects on KPM-induced particle transport since the plasma flow can influence the amplitude of density fluctuation and the radial velocity fluctuation as well as their cross-phase. We are just at the beginning studying the CM observed on EAST, and in order to understand the transport mechanism of the CM more work needs to be done, including: (1) is it the $E \times B$ convection or the magnetic component that contributes to particle transport, and (2) how does the CM interplay with the plasma flow and how does this interplay influence the CM-induced particle transport?

In summary, the CM in pedestal region on EAST has been observed in density, electron temperature and magnetic fluctuations. Poloidal asymmetry of the local poloidal wavenumber for the CM has been observed and has been explained by assuming that the mode is flute-like, i.e. $k_{//} \sim 0$. Based on this flute-like assumption, the toroidal mode number of the CM has been estimated as being between 12 and 17. In addition, the poloidal distribution of the amplitude of CM density fluctuation demonstrates a ballooning structure. Further analysis shows that as the CM mode amplitude increases, the rate of increase of the edge density decreases and the particle flux onto the divertor increases. The CM usually shows a bursty nature and CM bursts can lead to bursts of the particle flux onto the divertor with a time of about 230 $\mu$s, which is close to the time for particle flow from outer midplane to the divertor targets along the SOL magnetic field line. The analysis of density profiles shows that the existence of a CM mode can reduce the pedestal density and the density gradient. This suggests that the CM can drive outward particle transport.

## Acknowledgments

## References

[1] Doyle E J *et al* 2007 Progress in the ITER physics basis chapter 2: plasma confinement and transport *Nucl. Fusion* **47** S18
[2] Kinsey J E *et al* 2003 *Nucl. Fusion* **43** 1845
[3] Kinsey J E *et al* 2011 *Nucl. Fusion* **51** 083001
[4] Stacey W M 2004 *Phys. Plasmas* **11** 1511
[5] Callen J D *et al* 2010 *Nucl. Fusion* **50** 064004
[6] Groebner R J *et al* 2009 *Nucl. Fusion* **49** 045013
[7] Groebner R J *et al* 2010 *Nucl. Fusion* **50** 064002
[8] Burckhart A *et al* 2010 *Plasma Phys. Control. Fusion* **52** 064002
[9] Snyder P B 2009 *Phys. Plasmas* **16** 056118
[10] Snyder P B *et al* 2011 *Nucl. Fusion* **51** 103016
[11] Dickinson D *et al* 2011 *Plasma Phys. Control. Fusion* **53** 115010
[12] Dickinson D *et al* 2012 *Phys. Rev. Lett.* **108** 135002
[13] Hatch D R *et al* 2016 *Nucl. Fusion* **56** 104003
[14] Yan Z *et al* 2011 *Phys. Rev. Lett.* **107** 055004
[15] Diallo A *et al* 2014 *Phys. Rev. Lett.* **112** 115001
[16] Diallo A *et al* 2015 *Phys. Plasmas* **22** 056111
[17] Laggner F M *et al* 2016 *Plasma Phys. Control. Fusion* **58** 065005
[18] Zhong W L *et al* 2016 *Plasma Phys. Control. Fusion* **58** 065001
[19] Gao X *et al* 2013 *Plasma Sci. Technol.* **15** 732
[20] Gao X *et al* 2015 *Nucl. Fusion* **55** 083015
[21] Liu H Q *et al* 2014 *Rev. Sci. Instrum.* **85** 11D405
[22] Han X *et al* 2014 *Rev. Sci. Instrum.* **85** 073506
[23] Zhang S *et al* 2014 *Plasma Sci. Technol.* **16** 311
[24] Wang Y M *et al* 2013 *Fusion Eng. Des.* **88** 2950
[25] Qu H *et al* 2015 *Plasma Sci. Technol.* **17** 985
[26] Lee J *et al* 2014 *Rev. Sci. Instrum.* **85** 063505
[27] Wang L *et al* 2013 *Nucl. Fusion* **53** 073028
[28] Groebner R J *et al* 2001 *Nucl. Fusion* **41** 1789
[29] Mazurenko A *et al* 2002 *Phys. Rev. Lett.* **89** 225004

[30] Burrell K H *et al* 2005 *Phys. Plasmas* **12** 056121
[31] Snipes J A *et al* 2001 *Plasma Phys. Control. Fusion* **43** L23
[32] Burrell K H *et al* 2009 *Nucl. Fusion* **49** 085024
[33] Liu F *et al* 2015 *Nucl. Fusion* **55** 113002